PAPER

Check for updates

Towards a theoretical understanding of excitonic properties of phthalocyanine thin films. I. Low-temperature exciton absorption spectra

Sanghita Sengupta, [ID] *[ag] Zheng Pei, [ID] [ag] Chance Lander, [ID] [a] Carly R. Wickizer, [ID] [a] Yu Homma, [ID] [b] Hadi Afshari, [ID] [c] Yuezhi Mao, [ID] [d] Pengfei Huo, [ID] [e] Yu Zhang, [ID] [f] Sergei Tretiak, [ID] *[f] Lloyd A. Bumm, [ID] [c] Madalina I. Furis [ID] *[c] and Yihan Shao [ID] *[ag]

Phthalocyanine (Pc)-based molecular thin films have emerged in recent years as a promising class of organic semiconductor materials for optoelectronic applications owing to their long exciton coherence length and fast exciton diffusion. However, the dependence of their exciton properties on the dimensionality and thermodynamic conditions, presence of metal ions, and effects of chemical modifications to the PC systems is not yet fully understood. As a first step towards a more comprehensive theoretical understanding of the excitonic properties of Pc thin films, we model their low-temperature exciton absorption spectra by employing the Frenkel Hamiltonian. The latter is derived from quantum-chemical estimates of site energies and exciton–exciton couplings. The predicted exciton absorption spectra of octabutoxy phthalocyanine (H_2OBPc) is found to be strongly dependent on the dimensionality of the model as well as the distance cutoff for including the monomer–monomer exciton coupling. We also caution that the widely used dipole–dipole approximation could substantially overestimate the excitonic coupling between different monomers compared to a more accurate evaluation using the respective transition densities.

1 Introduction

Thin films composed of π-conjugated organic molecules are highly versatile materials, providing a robust platform for both fundamental photophysical studies and practical device applications. Their unique optical and electronic properties make them suitable for a range of optoelectronic technologies, including organic light-emitting diodes (OLEDs), organic photovoltaic cells (OPVs), and organic field-effect transistors (OFETs).[1–15] A key feature that underscores their applications is their unique ability to support long-distance energy transport *via* excitons, in addition to charge transport.[14,16–20]

At the microscopic level, the structural and electronic properties of these organic materials are primarily controlled by the nature of the intermolecular interactions.[5,9,20] In crystals of uncharged aromatic organic molecules, these interactions are predominantly π–π and van der Waals dispersion.[21,22] In contrast, Coulomb interactions between excitons on neighboring molecules enable exciton delocalization across multiple molecules, giving rise to coherent excitonic states that can diffuse in three dimensions.[23] As such, a combination of structural adaptability and efficient energy transport underpins the performance of many thin-film-based organic-optoelectronic devices.[24] One example is non-peripheral octabutoxy phthalocyanine (H_2OBPc) (Fig. 1(a)) which crystallizes in the $P\bar{1}$ triclinic system. It has a two-molecule basis where the two molecules are related by inversion symmetry, Fig. 2 (and SI Section S1 for more details). The molecules are organized into layers of π–π interacting molecules in the *ab* plane with the Pc rings tilted with respect to the plane. The layers then stack along the *c* axis. The interaction between the layers is predominantly the van der Waals interactions between the alkoxy chains.

Despite their remarkable features, organic molecular thin films remain poorly understood when it comes to the factors governing their static and dynamic properties. This limited understanding has hindered their widespread applications as

[a] *Department of Chemistry & Biochemistry, University of Oklahoma, Norman, OK 73019, USA*

[b] *Research Center for Organic Electronics (ROEL), Yamagata University, Jonan 4-3-16, Yonezawa, Yamagata 992-8510, Japan*

[c] *Homer L. Dodge Department of Physics, University of Oklahoma, Norman, OK 73019, USA. E-mail: madalina.furis@ou.edu*

[d] *Department of Chemistry and Biochemistry, San Diego State University, San Diego, CA 92182, USA*

[e] *Department of Chemistry, University of Rochester, Rochester, NY 14627, USA*

[f] *Theoretical Division and Center for Integrated Nanotechnologies, Los Alamos National Laboratory, Los Alamos, NM 87545, USA. E-mail: serg@lanl.gov*

[g] *Department of Chemistry, Brandeis University, Waltham, MA 02453, USA. E-mail: ssengupta@brandeis.edu, yihanshao@brandeis.edu*
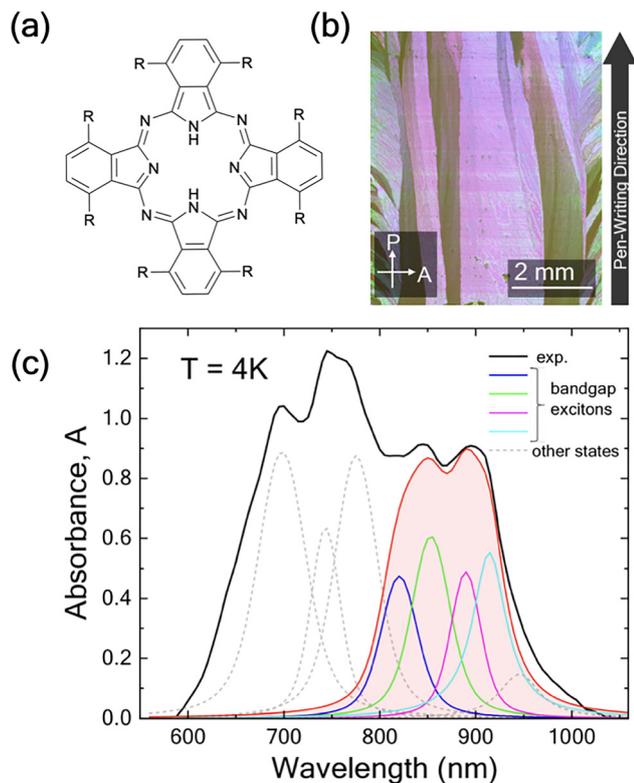
This journal is © the Owner Societies 2026

Phys. Chem. Chem. Phys., 2026, **28**, 7021–7034 | 7021

Fig. 1 (a) Molecular structure of H_2OBPc, R = $-O(CH_2)_3CH_3$. (b) Cross-polarized optical microscope image of an H_2OBPc crystalline thin film deposited through the meniscus-guided technique.[22] (c) Low-temperature (T = 4 K) absorbance (black line) recorded from the largest crystalline grain in (b). Contributions from several excitonic states are identified through a fitting procedure.[26] The contributions of the four near-bandgap excitonic states are highlighted in color.
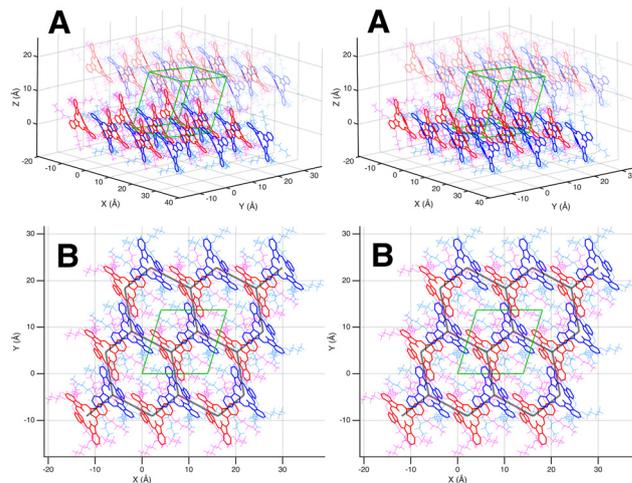

Fig. 2 Three-dimensional perspective of the molecular arrangement in the H_2OBPc crystal structure given by parallel-view stereo pairs. (A) A view of a 3 × 3 × 2 tiling of unit cells. The molecules are arranged in layers of π−π interacting molecules (*ab* plane). The layers are stacked in the *c* axis interacting by the alkyl chain van der Waals interactions and longer-range π−π interactions. The unit cell from the literature is shown in green,[39] which includes the lower half of the upper layer and the upper half of the lower layer. Here the *a* axis is aligned with the Cartesian *x* axis and the *b* axis is in the *xy* Cartesian plane. The triclinic P$\bar{1}$ unit cell contains two molecules related by inversion symmetry. These two molecules are distinguished by color. For clarity, the Pc rings are rendered in bold red and blue. The associated alkoxy chains are magenta and cyan, respectively. The upper layer is rendered with reduced opacity for clarity. (B) A view of a single layer in the ab plane tiled 3 × 3 × 1 showing the arrangement of the Pc rings in the distorted hexagonal lattice. The lower ab face of the unit cell from (A) is shown. Note that the [1$\bar{1}$0] lattice direction (the short *ab* face diagonal) lies in the plane of the Pc rings. The [111] direction (long body diagonal) is perpendicular to the plane of the Pc rings. The hexagonal lattice connecting the centers of the Pc rings is shown in thick gray lines.

optoelectronic materials, where precise control over molecular packing, exciton dynamics, and charge transport is crucial for optimal device performance. In the case of oriented mol thin films—whose crystallinity is illustrated in Fig. 1(b)—recent experimental advancements in the fabrication of macroscopically ordered crystalline films have unveiled clear signatures of delocalized, Wannier-like excitonic states formed at low temperatures.[22,25–27] Most notably, these excitonic states are characterized by low binding energies ($\sim$30–50 meV), a blue shift of excitonic energy with increasing temperature, and very intense sub-nanosecond radiative recombination at T = 4 K.[22,25–27] From a static perspective, it remains unclear how peripheral functionalization of the organic molecules modulates the crystal lattice structure and, in turn, how such crystal packing variations affect both the dimensionality and degree of delocalization of coherent excitonic states. The extent of this delocalization is often characterized by the exciton coherence length (L_{coh}), which quantifies the spatial extent of individual molecular units participating in a coherent exciton state. On the other hand, it is equally unclear how dynamical properties [*e.g.* exciton diffusion coefficient ($\mathscr{D}$), exciton lifetime (τ), and ultimately the exciton diffusion length $(\propto \sqrt{\mathscr{D}\tau})$] are impacted by local (molecular) and global (lattice) thermal fluctuations.

Complementary to experimental techniques, such as X-ray crystallography and ultrafast spectroscopy, the aforementioned two major challenges have been addressed with theoretical and computational modeling. The coherent exciton states in organic molecular thin films are known to be well described by the Frenkel–Davydov exciton model.[28] The effects of dynamic disorders in such systems have been modeled primarily through the Frenkel–Davydov–Holstein–Peierls model, which factors in how phonon modes modulate the exciton energies of individual molecules (Holstein coupling) and the exciton coupling between neighboring molecules (Peierls coupling).[29–31] Alternatively, dynamic disorders have been captured through atomistic molecular dynamics simulations at certain thermodynamic conditions.[32]

Inspired by these theoretical advances, especially (a) the 1D modeling of H_2OBPc thin films by Fornari, Aragó, and Troisi,[29] and (b) recent reports on the significance of model dimensionality and longer-range Coulomb interactions on the excitonic properties of other organic semiconductor systems,[30,31] here we undertake a comprehensive re-examination of the excitonic properties of the H_2OBPc thin films through a series of theoretical and computational modeling efforts. In the long term, our goal is to help unravel chemical-composition → crystalline-

7022 | *Phys. Chem. Chem. Phys.*, 2026, **28**, 7021–7034

This journal is © the Owner Societies 2026

structure → exciton-properties relationships, thereby providing guidance for the development of phthalocyanine (Pc) analogs that maximize the exciton coherence length and energy diffusion in organic thin films. As the first step in this direction, this work focuses on predicting the low-temperature exciton absorption spectra of H_2OBPc thin films with the aim of answering three simple but fundamental questions: (a) how does the dimensionality of the modeling (1D *vs.* 2D *vs.* 3D) affect the predicted excitonic properties? (b) does long-range Coulomb coupling between H_2OBPc molecules (beyond nearest neighbor approximation) contribute substantially to the exciton properties? and (c) how reliable is the dipole–dipole approximation for computing the Coulomb coupling compared to a more accurate approach based on exciton transition densities?

Our paper is organized as follows. In Section 2, we introduce the Davydov–Frenkel–Holstein–Peierls Hamiltonian, which is subsequently reduced to the Davydov–Frenkel Hamiltonian, suitable for modeling low-temperature behavior in the absence of phonon excitations. Section 3 outlines the computational framework used to extract interaction parameters *via* first-principles time-dependent density functional theory (TD-DFT) simulations and describes the tight-binding approach for constructing the Hamiltonian of molecular aggregates with varying dimensionalities and distance cutoffs. We also simulate low-temperature absorption spectra using a Voigt profile. The experimental procedure for acquiring absorption spectra in Fig. 1(c), along with the spectral peak fitting, is detailed in Section 3.4. Results from TD-DFT calculations are summarized in Section 4. A comparison of simulated and experimental absorption spectra across different aggregate models is discussed in Section 5. Finally, Section 6 summarizes our key findings and suggests possible extensions to incorporate finite-temperature effects.

2 Theoretical framework: model Hamiltonian for excitons

We consider a model organic semiconductor consisting of N sites (molecules), each having K excitonic states and coupled to a single phonon mode. The excitonic behavior of this system can be well described by the Frenkel–Davydov–Holstein Hamiltonian,[28,33–38]

$$H = \sum_{n=1}^{N} \sum_{k=1}^{K} \delta E_k c_{nk}^{\dagger} c_{nk} + \sum_{n=1}^{N} \sum_{k=1}^{K} \sum_{m \neq n}^{N} \sum_{l=1}^{K} J_{nk,ml} c_{nk}^{\dagger} c_{ml}$$
$$+ \hbar\omega_0 \sum_{n=1}^{N} \left(b_n^{\dagger} b_n + \frac{1}{2} \right) + \hbar\omega_0 \lambda \sum_{n=1}^{N} \sum_{k=1}^{K} \left(b_n + b_n^{\dagger} \right) c_{nk}^{\dagger} c_{nk},$$
$$(1)$$

where the first term involves the on-site energy δE_k, including molecular excitation energies and potential gas-to-crystal shifts. The operators $c_{nk}^{\dagger}$ and c_{nk} denote excitonic creation and annihilation operators, respectively, for the k-th exciton on the n-th site. The second term describes exciton hopping between sites n and m, with $J_{nk,ml}$ as the coupling constant

(either Coulomb coupling J_C or dipole–dipole coupling J_D). The third term accounts for phonon energy with ω_0 as the frequency, $b_n^{\dagger}$ and b_n as the phonon creation and annihilation operators for the n-th site. Finally, the fourth term factors in exciton–phonon coupling within the Holstein formalism, with λ as the coupling constant, introducing corrections to the on-site energy.

This study employs the low-temperature approximation described in Section 1, where the phonon-related terms are neglected. As a result, eqn (1) reduces to the Frenkel exciton Hamiltonian,

$$H = \sum_{n=1}^{N} \sum_{k=1}^{K} \delta E_k c_{nk}^{\dagger} c_{nk} + \sum_{n=1}^{N} \sum_{k=1}^{K} \sum_{m \neq n}^{N} \sum_{l=1}^{K} J_{nk,ml} c_{nk}^{\dagger} c_{ml} \qquad (2)$$

Here parameters such as excitation energies (δE_k) and coupling constants ($J_{nk,ml}$) can be directly obtained from first-principle calculations (Section 4), and subsequently incorporated into eqn (2). Diagonalization of the Hamiltonian matrix yields eigenvalues, E_i, and eigenvectors, $v_{nk,i}$, which are then used to simulate the exciton absorption spectra.

3 Computational & experimental methodology

Our computational methodology includes two main steps, (i) the extraction of excitation energies and other relevant parameters from TD-DFT calculations, and (ii) implementation of a tight-binding formalism to solve the Hamiltonian given in eqn (2). The following subsections detail each step.

3.1 Excited state calculations of molecular monomers and dimers

Excited state calculations for H_2OBPc monomer and dimers were performed using the TD-DFT formalism[40,41] within the Q-Chem software package.[42,43] Several standard functionals, including PBE,[44] PBE0,[45,46] LRC-ωPBE,[47] and ωB97X-D,[48] were employed with the 6-31G(d,p) basis set;[49–51] however, only the results from PBE0 were presented in the following main text for the sake of clarity whereas the rest were provided in SI. The basis set dependence of the on-site energies, transition dipole moments, and Coulomb couplings were benchmarked with PBE0 and provided in Tables S1 and S2. The transition densities were computed using the libwfa package[52] as implemented in Q-Chem.

To obtain structures of molecular monomer and dimers used for TD-DFT calculations, we first extracted unit cell parameters[39] and atomic coordinates from a standard crystallographic information file (CIF) of H_2OBPc as shown within a 3D representation in Fig. 2 (and SI Section S1 for more details), including two molecules in a unit cell with inversion symmetry. The relevant dimers were identified based on the inter-monomer distance (D_d) between the centers of mass of each monomer as shown in Fig. 3(b). The obtained structures were then subjected to TD-DFT calculations to evaluate the following key parameters: excitation energies for the monomer's Q_x and Q_y states,
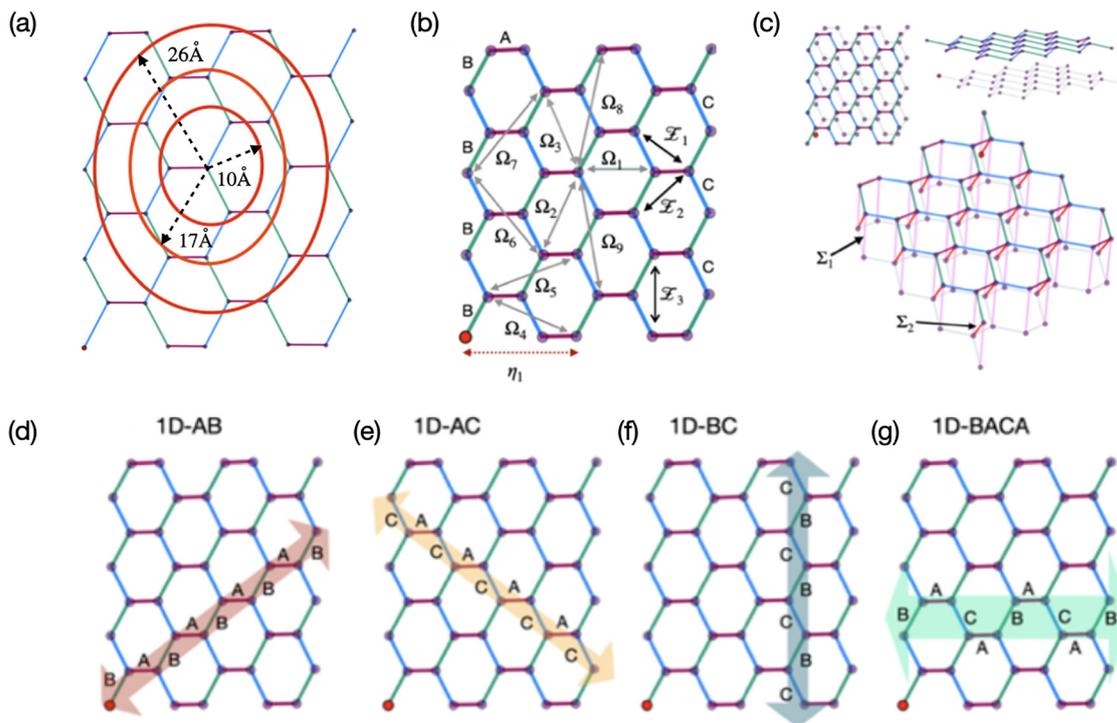
This journal is © the Owner Societies 2026

Phys. Chem. Chem. Phys., 2026, **28**, 7021–7034 | 7023

Fig. 3 Analysis of the molecular arrangement in the H_2OBPc crystal. (a) Top view of a 2D layer of the crystal, which corresponds to the xy-plane in Fig. 2(b) and shows three cutoff distances. (b) In the distorted hexagonal lattice, there are three types of nearest neighbors: A (7.43 Å, magenta line), B (9.741 Å, green line), and C (9.903 Å, blue line) within a cutoff distance of 10 Å; three types of second-nearest neighbors (shown in black solid lines): $\mathscr{L}_1$ (14.013 Å), $\mathscr{L}_2$ (14.309 Å), and $\mathscr{L}_3$ (16.936 Å), all within a cutoff distance of 17 Å. Also shown are nine third-nearest neighbors (gray solid line): Ω_1 (15.873 Å), Ω_2 (18.181 Å), Ω_3 (18.807 Å), Ω_4 (20.131 Å), Ω_5 (20.62 Å), Ω_6 (23.1 Å), Ω_7 (23.323 Å), Ω_8 (25.795 Å) and Ω_9 (25.98 Å) and one fourth-nearest neighbor η_1 (22.703 Å, red dotted line) which fall within 26 Å. (c) Top, side, and tilted views of two layers of the distorted hexagonal lattice of H_2OBPc with the two shortest interlayer distances: Σ_1 (16.907 Å, pink line) and Σ_2 (14.517 Å, red line). For clarity, only the center-of-mass of each molecule is shown. (d)–(g) Four different 1D models (highlighted with arrows) of H_2OBPc: zig-zag orientations of the 1D-AB, 1D-AC, 1D-BC models; 1D-BACA arm-chair model.

representing nearly degenerate excited states oriented along orthogonal directions within the molecular plane, see Fig. 1(a) and Fig. 4; the corresponding transition dipole moment vectors; and excitonic coupling terms for various dimers in Fig. 3(b). These intermolecular coupling terms could be calculated using either of the two approaches below. In the point dipole approximation, the interaction can be modeled as occurring between two transition dipole moments located at the centers of mass of each molecule in the dimer. This method is computationally efficient but assumes a simplified interaction that may neglect important spatial and electronic details. Alternatively, a more rigorous approach that involves evaluating the electrostatic Coulomb interaction between the transition densities associated with the excited states of each molecule in the pair can be employed. This method enables a more accurate and physically realistic assessment of exciton–exciton interactions, particularly for closely spaced molecules where the point dipole approximation may fail. The Q-Chem package includes an implementation of this methodology, dubbed as the direct coupling scheme,[53] which we employed in this study. Note that the Coulomb coupling can be further approximated by representing the transition densities as transition density cubes[54] or atomic transition charges.[32,55,56]

3.2 Tight-binding formalism for molecular thin films

In the tight-binding Hamiltonian matrix representation of a system with N H_2OBPc molecules, the diagonal elements of the resulting $2N \times 2N$ matrix correspond to the on-site excitation energies, where each molecule contributes two excitonic states, Q_x and Q_y. The off-diagonal elements capture the excitonic couplings, J, between pairs of molecules that lie within a predefined distance cutoff. These quantities were obtained from TD-DFT calculations and the couplings might correspond to either approximate dipole–dipole interactions or the more accurate direct Coulomb couplings. Eqn (3) exemplifies the structure of the Hamiltonian matrix for a system consisting of 3 or more molecules,

$$\mathbf{H} = \begin{pmatrix} Q_{x,11} & 0 & J_{xx,12} & J_{xy,12} & 0 & 0 & \cdots \\ 0 & Q_{y,11} & J_{yx,12} & J_{yy,12} & 0 & 0 & \cdots \\ J_{xx,21} & J_{xy,21} & Q_{x,22} & 0 & J_{xx,23} & J_{xy,23} & \cdots \\ J_{yx,21} & J_{yy,21} & 0 & Q_{y,22} & J_{yx,23} & J_{yy,23} & \cdots \\ 0 & 0 & J_{xx,32} & J_{xy,32} & Q_{x,33} & 0 & \cdots \\ 0 & 0 & J_{yx,32} & J_{yy,32} & 0 & Q_{y,33} & \cdots \\ \cdots & \cdots & \cdots & \cdots & \cdots & \cdots & \cdots \end{pmatrix},$$

(3)

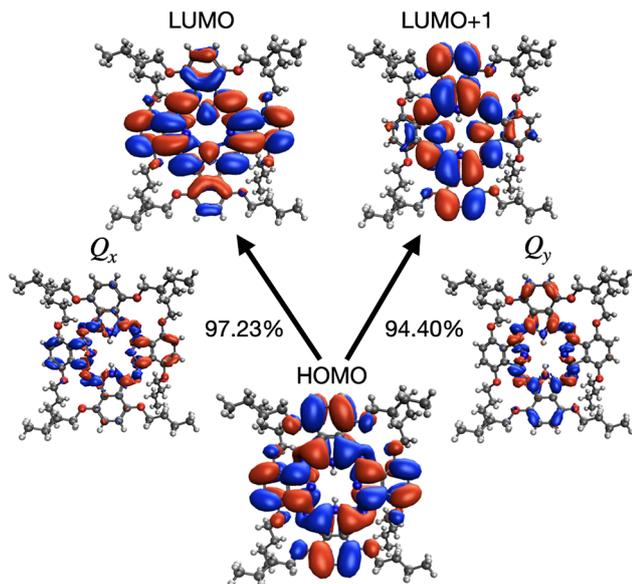where two pairs of molecules (1,2) and (2,3) lie within the distance cutoff, while the (1,3) pair does not.

7024 | *Phys. Chem. Chem. Phys.*, 2026, **28**, 7021–7034

This journal is © the Owner Societies 2026

PCCP

Paper

Fig. 4 Frontier molecular orbitals (HOMO, LUMO, and LUMO+1) and transition densities of the Q_x and Q_y excited states of H_2OBPc, obtained from DFT and TD-DFT calculations, respectively, at the crystal monomer geometry using the PBE0 functional and 6-31G(d,p) basis. The percentages indicate the weights of the dominant single-particle excitations (HOMO → LUMO or HOMO → LUMO+1) to the Q_x and Q_y states. The isosurface values for molecular orbitals and transition densities are set to 0.02 and 0.001, respectively.

The tight-binding models were further constructed to explore different dimensionalities (1D, 2D, and 3D) by applying three distance cutoffs, r_{cut} = 10, 17, 26 Å, labeled as "1NN-10 Å", "2NN-17 Å", and "3NN-26 Å", respectively. In Fig. 3(b), all nearest neighbors (dimers A, B, and C) were located within a center-to-center distance of 10 Å. The 17 Å cutoff extended the interaction range to include all second-nearest neighbors ($\mathscr{L}_1$, $\mathscr{L}_2$, $\mathscr{L}_3$) as well as one third-nearest neighbor (Ω_1). Expanding the cutoff further to 26 Å incorporated additional third-nearest neighbor interactions (Ω_2 through Ω_9) and one fourth-nearest neighbor coupling η_1. This hierarchical inclusion of longer-range interactions enables a more complete modeling of exciton delocalization and collective optical response across increasing dimensionality and coupling patterns within the molecular crystal.

In the 1D models, molecules are aligned in a chain-like structure highlighted as arrows in Fig. 3(d)–(g). For example, the 1D-AB model in Fig. 3(d) incorporates only the nearest neighbor interactions for A and B dimers with the "1NN-10 Å" cutoff, while the second-nearest neighbor interactions for $\mathscr{L}_2$ dimers are added to the "2NN-17 Å" cutoff, and the "3NN-26 Å" cutoff includes dimers Ω_5 and Ω_7. Similarly, the "2NN-17 Å" cutoff adds $\mathscr{L}_1$ dimers to the 1D-AC model (Fig. 3(e)), $\mathscr{L}_3$ dimers to the 1D-BC model (Fig. 3(f)), and $\mathscr{L}_1$, $\mathscr{L}_2$, and Ω_1 dimers to the 1D-BACA model (Fig. 3(g)), in addition to the corresponding nearest neighbors.

In 2D systems, molecules are arranged in a planar grid within a single layer, with intermolecular distances defined in Fig. 3(b). This planar layout supports strong in-plane excitonic

interactions, capturing the characteristics of two-dimensional molecular aggregates. In contrast, 3D systems incorporate multiple layers, which are stacked on top of each other as shown in Fig. 3(c). This stacking results in a three-dimensional arrangement, where interactions occur both within individual layers and between adjacent layers (through the Σ_1- and Σ_2-dimer interactions illustrated in Fig. 3(c)), offering a comprehensive representation of the bulk molecular systems.

3.3 Simulation of absorption spectra

Our modeling of the absorption spectra relies on the computation of the spectral weight $A(\lambda)$ as a function of wavelength λ. To capture realistic spectral features, the absorption lines are broadened using a Voigt profile, representing a convolution of two broadening mechanisms, namely a Gaussian component typically associated with Doppler broadening due to thermal fluctuations or other inhomogeneous effects, as well as a Lorentzian component accounting for finite excited state lifetimes. The Voigt profile of a center λ_i is computed using the Faddeeva function $\omega(z) = e^{-z^2} \text{erfc}(-iz)$, given as

$$V_i(\lambda) = \frac{\text{Re}[\omega(z_i)]}{\sigma\sqrt{2\pi}}, \qquad (4)$$

with $z_i = [(\lambda - \lambda_i) + \text{Im}(\gamma_i)]/\sigma\sqrt{2}$, where γ_i corresponds to the width in Lorentzian function $\mathscr{L}_i(\lambda) \propto \gamma_i/\pi[(\lambda - \lambda_i)^2 + \gamma_i^2]$, and σ comes from the Gaussian distribution $\mathscr{G}_i(\lambda) \propto \exp(-(\lambda - \lambda_i)^2/2\sigma^2)$ that captures inhomogeneous effects.

It is well established that TD-DFT simulations based on different density functional approximations can exhibit systematic errors in excitation energies, often underestimating or overestimating absolute values depending on the choice of functional. Consequently, we introduce an energy shift correction ΔE_{shift}, in order to align the computational results with the experimental peak positions and spectral tails more accurately. Accordingly, the transition wavelength of i-th excitonic state is modified as,

$$\lambda_i = \frac{hc}{E_i - \Delta E_{shift}}, \qquad (5)$$

where E_i is the obtained eigenstate energy, h is the Planck's constant in eV s, and c is the speed of light in m s^{-1}.

We also use the oscillator strength f_i to weigh the Voigt profile that scales the contribution of each electronic transition to the overall absorption spectrum, which is calculated as,

$$f_i = \frac{2}{3}E_i \sum_{nk,ml} v_{nk,i}v_{ml,i}\vec{T}_k \cdot \vec{T}_l = \frac{2}{3}E_i \left| \sum_{nk} v_{nk,i}\vec{T}_k \right|^2, \qquad (6)$$

where $v_{nk,i}$ are components of the eigenvector of the Frenkel Hamiltonian in eqn (2) corresponding to the i-th eigenvalue, and $\vec{T}_k$ and $\vec{T}_l$ represent the transition dipole moment vector of the k- and l-th excited state of each monomer, respectively.

This journal is © the Owner Societies 2026

Phys. Chem. Chem. Phys., 2026, **28**, 7021–7034 | **7025**

Finally, we sum over all transitions to get the total absorption spectra,

$$A(\lambda) = \sum_i f_i V_i(\lambda). \tag{7}$$

3.4 Absorption measurement and spectral fitting

The simulated absorption spectra were compared with the experimental absorption measurements performed at $T = 4$ K of H_2OBPc crystalline thin film fabricated using a meniscus-guided, solution processing deposition technique known as pen-writing.[57–60] Briefly, a glass capillary, loaded with a 0.5% H_2OBPc solution in toluene, is translated at a speed of 20 μm s^{-1} onto a dielectric substrate (e.g. glass, indium tin oxide (ITO), or sapphire). At this speed, nucleation takes place exclusively at the line of contact between the solution meniscus and the substrate, resulting in a film morphology that features long macroscopic grains, as evidenced by the cross-polarized optical microscope image in Fig. 1(b). The contrast between grains observed in this figure originates from the different orientation of crystalline axes and excitonic dipoles in neighboring grains. Extensive grazing incidence X-ray diffraction, absorbance, and linear dichroism studies established that the films are crystalline with the c-axis oriented out of the plane of the substrate.[22,25,27]

Low temperature absorbance is measured at normal incidence using a quasi-monochromatic tunable light source composed of a tungsten halogen lamp and a grating monochromator. Light is focused onto the sample to a diameter less than 100 μm using a short focal length achromat lens, and positioned inside the largest grain using an in situ sample viewing telescope. For low-temperature measurements the sample is placed inside a closed cycle refrigerator. The transmitted light is detected using an amplified Si detector coupled with a locking amplifier. A typical 4 K absorption spectrum is presented in Fig. 1(c) (black line).

A peak-fitting procedure following the protocol reported by Liang et al. in ref. 27 reveals eight distinct contributions to the absorption, among which four near-bandgap excitations originate from the Q_x and Q_y molecular excitations involving HOMO → LUMO and HOMO → LUMO+1 transitions. The remaining four higher-energy excitonic states are associated with HOMO → LUMO+n ($n > 1$) transitions. The present work exclusively focuses on the former four excitonic states, highlighted in color in Fig. 1(c). Previous study[27] has isolated the contributions of the bandgap excitons using low-temperature magnetic circular dichroism (MCD) and linear dichroism (LD) measurements (see SI of ref. 27 for more details). The same work has also reported that all four transition excitonic dipoles are linearly polarized in the plane of the substrate. Our peak fitting routine considers the same energies for the near-bandgap excitons as those reported in ref. 27. Among the four states in question, the lowest-energy excitonic transition is of particular interest due to its distinct evolution with increasing temperature, associated with the formation of a delocalized state.

4 Electronic structure of H_2OBPc monomer and dimers

In this section, we analyze the TD-DFT results of H_2OBPc monomer and dimers, which provided the on-site excitation energies and the exciton–exciton couplings necessary for constructing the model Hamiltonian in eqn (3) for systems of varying dimensionalities.

4.1 Molecular orbitals and transition densities

There is a critical interplay between orbital symmetries and electronic excitations, which defines the optoelectronic properties of the H_2OBPc system. Fig. 4 displays the frontier molecular orbitals (MOs) and transition densities of the near-degenerate Q_x and Q_y states (from PBE0 functional as a representative with an energy difference of 73 meV). Across all the four functionals examined (Fig. S2), several consistent trends emerge: (i) the HOMO shows delocalized π-electron character over the central macrocycle and serves as the primary donor orbital in the two low-lying electronic excitations; (ii) the LUMO and LUMO+1 orbitals display complementary delocalization patterns and their symmetries (B_{2g} and B_{3g} if the monomer had a perfect D_{2h} symmetry) differ from that of the HOMO (A_u), thus making them orthogonal to the HOMO; (iii) transition density for the Q_x state (i.e. the first excited state) is dominated by the HOMO → LUMO transition and is mostly localized on the central macrocycle and extended to the periphery in one direction; and (iv) transition density for the Q_y state (i.e. the second excited state) involves the main contribution from the HOMO → LUMO+1 transition with its electronic density distribution extending to the peripheral substituents in another direction. These orbital trends are in agreement with Gouterman's four-orbital model,[61,62] which predicts the perpendicular transition dipole moments and near degenerate LUMO and LUMO+1 orbitals. While the LRC-ωPBE functional yields similar frontier orbital shapes as shown in Fig. S2(d), the resulting Q_x and Q_y states are less dominated by a single orbital pair excitation and the leading contributions are reversed. Furthermore, functional dependence of the excitation energies of Q_x and Q_y states of H_2OBPc and the transition dipole moments (T_x, T_y) are shown in Fig. S3, where the Q_x and Q_y states display the largest differences in the excitation energies with the PBE functional, a smaller difference with the PBE0 functional, and become nearly degenerate with the ωB97X-D and LRC-ωPBE functionals.

As far as the basis set dependence is concerned, Table S1 shows slightly lower on-site Q_x and Q_y excitation energies (up to 40 meV) with larger basis sets and the same functional (PBE0). However, the energy difference between these two states and their transition dipole moments (Table S1) and Coulomb couplings (Table S2) are all insensitive to the choice of basis set.

4.2 Exciton couplings from TD-DFT calculations at varying inter-molecular distances

In this section, we will focus on the key Frenkel Hamiltonian parameters, the excitonic coupling evaluated using two distinct
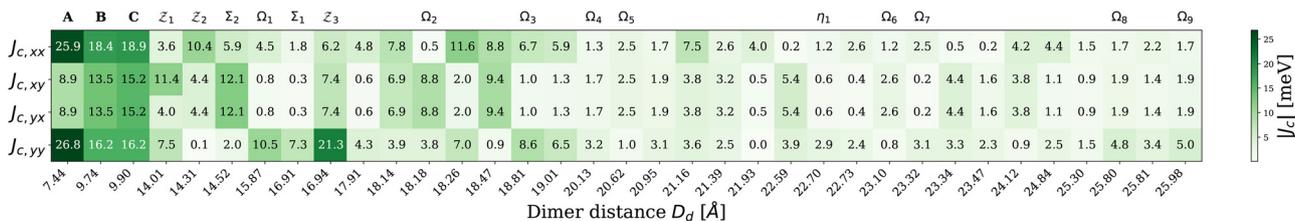
7026 | Phys. Chem. Chem. Phys., 2026, **28**, 7021–7034

This journal is © the Owner Societies 2026

	A	B	C	$\mathscr{Z}_1$	$\mathscr{Z}_2$	Σ_2	Ω_1	Σ_1	$\mathscr{Z}_3$				Ω_2				Ω_3	Ω_4	Ω_5				η_1		Ω_6	Ω_7							Ω_8		Ω_9
$J_{C,xx}$	25.9	18.4	18.9	3.6	10.4	5.9	4.5	1.8	6.2	4.8	7.8	0.5	11.6	8.8	6.7	5.9	1.3	2.5	1.7	7.5	2.6	4.0	0.2	1.2	2.6	1.2	2.5	0.5	0.2	4.2	4.4	1.5	1.7	2.2	1.7
$J_{C,xy}$	8.9	13.5	15.2	11.4	4.4	12.1	0.8	0.3	7.4	0.6	6.9	8.8	2.0	9.4	1.0	1.3	1.7	2.5	1.9	3.8	3.2	0.5	5.4	0.6	0.4	2.6	0.2	4.4	1.6	3.8	1.1	0.9	1.9	1.4	1.9
$J_{C,yx}$	8.9	13.5	15.2	4.0	4.4	12.1	0.8	0.3	7.4	0.6	6.9	8.8	2.0	9.4	1.0	1.3	1.7	2.5	1.9	3.8	3.2	0.5	5.4	0.6	0.4	2.6	0.2	4.4	1.6	3.8	1.1	0.9	1.9	1.4	1.9
$J_{C,yy}$	26.8	16.2	16.2	7.5	0.1	2.0	10.5	7.3	21.3	4.3	3.9	3.8	7.0	0.9	8.6	6.5	3.2	1.0	3.1	3.6	2.5	0.0	3.9	2.9	2.4	0.8	3.1	3.3	2.3	0.9	2.5	1.5	4.8	3.4	5.0
D_d [Å]	7.44	9.74	9.90	14.01	14.31	14.52	15.87	16.91	16.94	17.91	18.14	18.18	18.26	18.47	18.81	19.01	20.13	20.62	20.95	21.16	21.39	21.93	22.59	22.70	22.73	23.10	23.32	23.34	23.47	24.12	24.84	25.30	25.80	25.81	25.98

$|J_C|$ [meV]

Fig. 5 Absolute values of calculated Coulomb couplings, $J_{C,xx}$, $J_{C,xy}$, $J_{C,yx}$ and $J_{C,yy}$, at various distances between the molecular pairs (D_d) using the TD-DFT transition densities of Q_x and Q_y states within PBE0/6-31G(d,p) level of theory at the dimer structures extracted from crystal geometry. The plotted values correspond to the first-nearest neighbor (1NN, denoted by A, B, C), second-nearest neighbor (2NN, denoted by $\mathscr{Z}$'s) and third-nearest neighbor (3NN, denoted by Ω's) interactions, with η_1 being the sole fourth-nearest neighbor interaction within distance <26 Å. Two of the shortest interlayer interactions are shown as Σ_2 and Σ_1. The remaining unlabeled dimer distances correspond to other interlayer interactions.

approaches described above, namely, Coulomb coupling J_C and point-dipole approximation J_D. The results presented here use the PBE0/6-31G(d,p) level of theory for various dimer distances D_d. Additional results based on other density functionals are compiled in Fig. S5 of the SI.

Fig. 5 summarizes the computed Coulomb coupling constants between the two local excited-states in dimers, $J_{C,xx}$, $J_{C,xy}$, $J_{C,yx}$ and $J_{C,yy}$, at varying dimer distances (D_d). For the A-dimer, the $J_{C,xx}$ and $J_{C,yy}$ values (about 26 meV) are much stronger than $J_{C,xy}$ and $J_{C,yx}$ (less than 9 meV). For dimers B and C, on the other hand, the four couplings are more comparable in the range of 13–19 meV. As such, B- and C-dimers display weaker $J_{C,xx}$ and $J_{C,yy}$ couplings compared to the A-dimer but stronger $J_{C,xy}$ and $J_{C,yx}$ couplings. Considering that B- and C-dimers have slightly longer monomer–monomer distances compared to that in the A-dimer (9.74/9.90 Å vs. 7.44 Å), this reflects that the coupling strengths depend not only on the inter-monomer distances but also on the relative orientation of the monomer transition dipole moments.

In general, the coupling values shown in Fig. 5 for the second-nearest neighbors (dimers $\mathscr{Z}_1$, $\mathscr{Z}_2$, and $\mathscr{Z}_3$) are weaker than those for the nearest neighbors (A, B, and C), reflecting an expected decay of electrostatic interactions as the intermolecular distance increases. However, a simple d^{-3} decay is not observed. Specifically, $J_{C,xx}$ coupling of $\mathscr{Z}_2$-dimer is approximately 50% of those for the B- and C-dimers. For $J_{C,xy}$ and $J_{C,yy}$, both $\mathscr{Z}_1$ and $\mathscr{Z}_3$-dimers display rather strong couplings. For $J_{C,yx}$, $\mathscr{Z}_3$-dimer coupling appears to be strong as well. The Ω_1-dimer, the only third-nearest neighbor within a 17 Å distance cutoff, shows a notably strong $J_{C,yy}$ value. Between the layers, the Σ_2-dimer exhibits large $J_{C,xy}$ and $J_{C,yx}$ values ($\sim$ 12 meV) that are actually comparable to J-values of the A-, B-, and C-dimers. The Σ_1-dimer also shows a strong $J_{C,yy}$ coupling value while its other three couplings remain weak. These observations strongly suggest that the second-nearest neighbor and interlayer interactions might substantially affect the excitonic properties of H_2OBPc. In addition, many couplings of the third-neighboring dimers (Ω's) are non-negligible in the 17–26 Å inter-molecular distance; for example, dimers Ω_2 and Ω_3 come with some coupling values close to 10 meV.

Regarding the functional dependence, the couplings generally follow the trend: PBE < PBE0 < ωB97X-D < LRC-ωPBE, as shown in Fig. S5 in SI. This can be attributed to an increased fraction of the Hartree–Fock exchange along the functional sequence, which typically enhances the magnitudes of the transition dipoles (Fig. S3(b)). However, there are noticeable deviations, especially with the LRC-ωPBE functional, which produces relatively small off-diagonal coupling values for the A-dimer, a smaller $J_{C,xy}$ for the $\mathscr{Z}_1$- and Σ_2-dimers, smaller $J_{C,yx}$ value for the Σ_2-dimer, and smaller $J_{C,yy}$ for the $\mathscr{Z}_3$- and Σ_1-dimers. On the other hand, this functional also results in larger values for $J_{C,xx}$ for the $\mathscr{Z}_3$-dimer, $J_{C,xy}$ for the Σ_1-dimer, $J_{C,yx}$ for the $\mathscr{Z}_2$- and Σ_1-dimers, and $J_{C,yy}$ for the Σ_2-dimer. $J_{C,yx}$ for the $\mathscr{Z}_2$- and Σ_1-dimers, and a small $J_{C,yx}$ value for the Σ_2-dimer.

5 Exciton absorption spectra simulated across different dimensionalities

The aforementioned TD-DFT-derived parameters for various dimers were adopted into the Frenkel exciton Hamiltonian with eqn (3) to calculate the low-temperature absorption spectra following the steps outlined in Section 2. Specifically, we modeled exciton absorption spectra for multiple cases including the monomer and the three first-nearest neighboring dimers (shown in Fig. S7 and S8 with Coulomb couplings and dipole–dipole approximation, respectively), as well as 1D, 2D, and 3D models of the H_2OBPc thin film (in Fig. 6, 7, S9–S12, S14, and S15). To benchmark the various assumptions in our calculations, we compared our simulated spectra with experimental absorption spectra for polycrystalline, pen-written thin films of H_2OBPc from ref. 27. In our comparison of simulated and experimental spectra, an additional energy shift (ΔE_{shift}) wads employed to better mimic the experimental results. The physical origin of ΔE_{shift} could be related to the gas-to-crystal shifts, effects of vinyl stretching mode ω_0[33,37] (see eqn (1)), as well as systematic errors in the TD-DFT methods used for excited state description.[63] We optimized the energy shift parameter ΔE_{shift} to minimize the difference between theoretical and experimental spectral areas. While an objective function optimization would be ideal, the shift ΔE_{shift} was manually adjusted here, which should not introduce any qualitative difference.
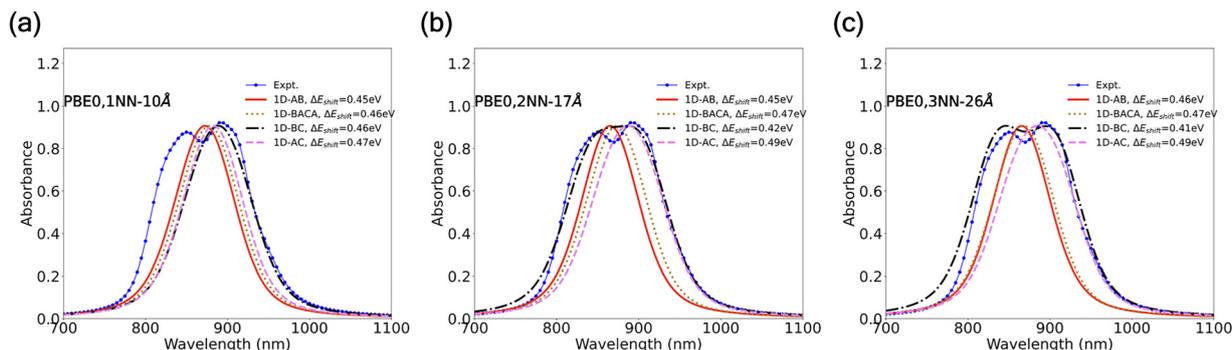
Fig. 6 Simulated exciton normalized absorption spectra for various 1D models in Fig. 3(d)–(g) of 600 H_2OBPc molecules using Coulomb couplings at (a) 10, (b) 17, and (c) 26 Å distance cutoffs from TD-DFT calculations within PBE0/6-31G(d,p) level of theory, against to the experimental spectra from ref. 27. (a) With a 10 Å distance cutoff, only the nearest-neighbor couplings (A, B, C in Fig. 3) are included. (b) When the cutoff is increased to 17 Å, all second-nearest neighbors ($\mathscr{L}_1$, $\mathscr{L}_2$, $\mathscr{L}_3$) and the third-nearest neighbor (Ω_1, only in the case of 1D-BACA) are also added to the Frenkel Hamiltonian. ΔE_{shift} corresponds to an additional shift (in nm) to better match the two experimental peaks. Gaussian broadening with σ = 25 nm and Lorentzian broadening with γ = 20 nm are applied in eqn (4).
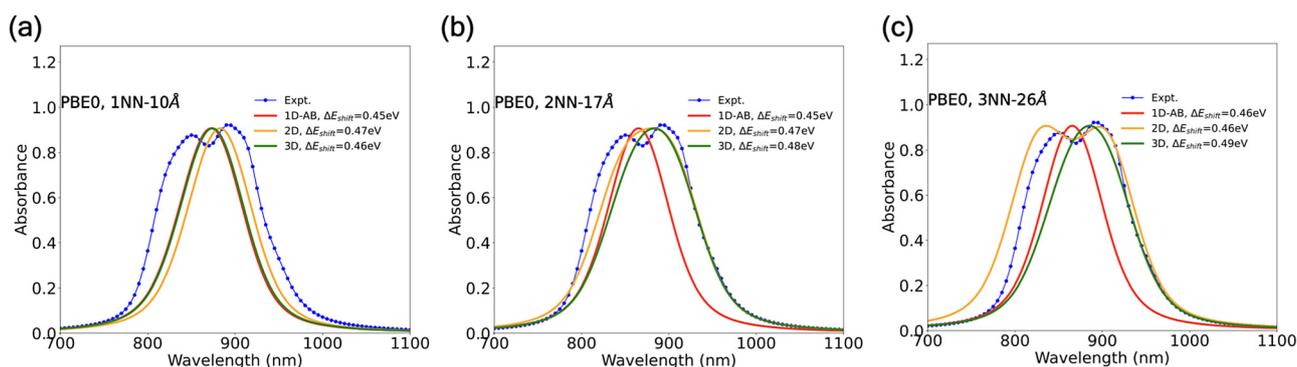
Fig. 7 Simulated exciton normalized absorption spectra of 600 H_2OBPc molecules from 1D-AB, 2D, and 3D models using Coulomb coupling (J_C) from TD-DFT PBE0/6-31G(d,p) calculations with broadening parameters σ = 25 nm and γ = 20 nm. Molecular arrangements considered: 1D chain with 600 molecules along the x-axis; 2D lattice with 60 molecules along x and 10 along y; and 3D lattice with 30 molecules along x, 10 along y, and 2 layers along z, yielding 600 molecules in each case. Panels (a), (b), and (c) show the evolution of the absorption spectra with increasing system dimensionality for distance cutoffs of 10, 17, and 26 Å, respectively. The 10 Å cutoff includes only nearest-neighbor couplings (A, B, and C); the 17 Å cutoff incorporates all second-nearest-neighbor interactions ($\mathscr{L}_1$, $\mathscr{L}_2$, and $\mathscr{L}_3$); and the 26 Å cutoff captures all third-nearest-neighbor couplings, along with one fourth-nearest-neighbor interaction, as illustrated in Fig. 3(b).

5.1 Exciton absorption spectra for molecular aggregates arranged in 1-dimension

The absorption spectra for four different 1D models—1D-AB, 1D-AC, 1D-BC, and 1D-BACA introduced in Fig. 3(d)–(g)—are shown in Fig. 6 and compared to the experimental spectra of the H_2OBPc thin film at 4 K.[27] For a comparison of absorption spectra across different functionals, see Section S8 and Fig. S9.

When only the nearest-neighbor interactions are considered (1NN-10 Å), the 1D-AB, 1D-AC and 1D-BACA models produce similar absorption spectra, while the 1D-BC arrangement results in a noticeably different absorption spectra, see Fig. 6(a). This difference arises because the B- and C-dimers share similar dimer distances (9.74 and 9.90 Å, respectively) and are both comprised of monomers with inverted symmetries. This is confirmed by the dimer spectra in Fig. S7 or S8, in which the B- and C-dimers give nearly identical absorption profiles with PBE0, ωB97X-D, and LRC-ωPBE functionals. Given these similarities, if

one approximates the B-dimer to be equivalent to the C-dimer, then 1D-AC and 1D-BACA are reduced to 1D-AB, and the three models would yield similar absorption spectra. Conversely, since 1D-BC does not contain an A-dimer, the 1D-BC adsorption spectra is expected to differ from that of 1D-AB. Nevertheless, these 1D models all generate single-peak spectra, contradicting to the experimentally two absorption peaks.

When the second- and third-nearest neighbor couplings are added (2NN-17 Å and 3NN-26 Å), shown in Fig. 6(b) and (c), the absorption spectra from the 1D models have no significant differences, except for 1D-BC (dashed black lines). In particular, the spectra of 1D-BC model show two distinct peaks and become closer to the experimental curves and a clear double-peaked profile is produced after all the third-neighbor interactions are included in panel (c). This clearly indicates the importance of including longer-range couplings in the exciton modeling.

7028 | *Phys. Chem. Chem. Phys.*, 2026, **28**, 7021–7034

This journal is © the Owner Societies 2026

5.2 Exciton absorption spectra across different dimensionalities simulated using direct Coulomb coupling

Adopting the formalism given in Section 3.2 and calculated Frenkel exciton Hamiltonian parameters (*i.e.*, J_C constants) analyzed in Section 4.2, we next explore the effect of dimensionality on the absorption spectra across different models (1D-AB, 2D, and 3D) encompassing aggregates of 600 H_2OBPc molecules. Among of the 1D arrangements studied, we focus on the 1D-AB model, at it was previously employed in an earlier study by Troisi and coworkers.[29] For the 3D model, the 600 molecules fall into two layers, each with 300 molecules. As shown in Fig. S14, the simulated adsorption spectra do not change substantially with more molecules for all three models and more layers for the 3D model (see panels (j)–(l) of Fig. S14). From the predicted absorption spectra in Fig. 7 and S10, several key observations can be made regarding the effect of dimensionality, density functional choice, and cutoff distance.

(i) Dimensionality: 1D aggregates (red curves in Fig. 7) consistently exhibit narrow spectral shape with 1NN-10 Å, 2NN-17 Å, and 3NN-26 Å models, as the excitonic couplings are confined to a single 1D chain of molecules. As the dimensionality increases from 1D to 2D (yellow curves), the spectra with PBE0 functional broaden substantially with 2NN-17 Å and 3NN-26 Å models, indicating the effect of including exciton couplings across the 2D plane. When the dimensionality increases further to 3D (green), there is a noticeable but much smaller change in the absorption spectra with the 1NN-10 Å and 2NN-17 Å models. This suggests that interlayer exciton couplings through Σ_1 and Σ_2 dimers play a relatively marginal role in the context of predicting low-temperature absorption spectra with these cutoff distances. For the 3NN-26 Å model, however, the 3D absorption spectra are appreciably different from the 2D case.

(ii) Functional dependence: while PBE and PBE0 calculations often lead to qualitatively similar spectral shapes (Fig. S10 and Fig. 7), PBE produces more pronounced spectral peaks compared to PBE0. This is attributed to differences in the excitation energies and transition dipole moments $T_{x/y}$ between the PBE and PBE0 approximations as seen in Fig. S3. On the other hand, the predicted absorption spectra of the 2D or 3D models with 17 and 26 Å distance cutoffs also look similar between the two long-range-corrected functionals (LRC-ωPBE and ωB97X-D) as shown in Fig. S10.

(iii) Cutoff radius: when the cutoff radius is increased from 10 to 17 Å, second-nearest neighbors are also considered for the exciton coupling. With the PBE0 functional, there is a noticeable broadening of the overall absorption spectra and, where visible, a larger splitting of the two predicted absorption peaks. This is expected and attributable to the inclusion of longer-range interactions. For other functionals, the dependence of absorption spectra on the cutoff radius is shown in Fig. S10.

(iv) Polarization-dependent absorption spectra: polarization dependence for the lowest absorption peaks for the 1D-AB, 2D, and 3D models using the Coulomb coupling considering different components of the transition dipole moment vector $\vec{T}$,

viz. x, y, or z are shown in Fig. S15. Appreciable changes in the spectra are observed for the different components of the transition dipole moments in the case of the 2D, 3NN-26 Å model.

(v) Comparison with experimental observation: at first glance, our results show the experimental double peak spectrum is better reproduced by the 1D-BC and 2D simulations (Fig. 6(c) and 7(c)), if longer-range interactions (3NN-26 Å) are included in the model and if using broadening parameters of $\sigma = 25$ nm and $\gamma = 20$ nm. It is, however, premature for us to state which combination of model dimensionality and density functional performs the best, as all predicted absorption spectra are subjected to energy shifts and line broadening empirical parameters. Fig. S16, for instance, illustrates the effects of Gaussian (σ) and Lorentzian (γ) broadening across all dimensionalities, including the 1D-AB, 1D-BC, 2D, and 3D models. Across these spectra, σ and γ tune two complementary broadening mechanisms with distinct visual signatures. Increasing γ (10–30 nm) enhances Lorentzian broadening, causing individual features to become wider and smoother and closely spaced peaks to merge. Increasing σ (5–25 nm) strengthens Gaussian broadening, leading to an overall spreading of the spectrum in which sharp differences between peaks are progressively reduced, while asymmetry and shoulder-like features persist and evolve. In addition to the aforementioned 1D-BC and 2D models, two distinct peaks also arise in Fig. S16(a)–(c) from 3D models with smaller σ and/or γ broadening values.

Intensity-wise, the experimental absorption spectrum shows peaks at 849 and 891 nm, where the latter is slightly higher in its intensity. In benchmarking studies,[64] the predicted peak intensities (including the relative strength between different peaks) were reported to be strongly dependent on the choice of the density functional. While such a functional dependence was indeed observed in our study, we found the predicted spectral shape to be also dependent on the dimensionality of the model and the broadening parameters. With our default choice of Gaussian ($\sigma = 25$ nm) and Lorentzian ($\gamma = 20$ nm) broadening, the absorption profiles from both 1D-BC model in Fig. 6(c) and 2D model in Fig. 7(c) show two peaks of nearly equal intensity with PBE0 functional and at 26 Å distance cutoff. An equal peak intensity can also be found in Fig. S16 with other broadenings, except for panel f ($\sigma = 15$ nm and $\gamma = 30$ nm) where the shorter-wavefunction peak has a noticeably lower intensity in the spectrum of 1D-BC model. The 3D modeling spectra with PBE0 functional in panels (a) and (b) of Fig. S16, on the other hand, do show the shorter-wavelength peak with a lower intensity. In Fig. S10(a)–(c), the 3D-model also leads to two peaks with the use of PBE functional, but the longer-wavelength peak has substantially lower intensity.

5.3 Exciton absorption spectra across different dimensionalities using dipole–dipole coupling

Fig. S12 shows the absorption spectra across different dimensionalities, functionals, and distance cutoffs, albeit simulated using the dipole–dipole coupling parameters J_D summarized in Fig. S6.

This journal is © the Owner Societies 2026

Phys. Chem. Chem. Phys., 2026, **28**, 7021–7034 | **7029**

Overall, J_D values are larger compared to their more accurate counterparts, J_C. As such, stronger J_D couplings lead to spectra with more pronounced peaks across all functionals, highlighting the long-range nature of dipole–dipole interactions, as shown in Fig. S5 and S6. Dimensional differences (1D-AB vs. 2D vs. 3D) are also more pronounced with J_D. In general, when the PBE functional is used, our absorption spectra in Fig. S12 modeled with the dipole–dipole couplings tend to overestimate the peak splittings relative to the experimental observations. [In addition, a subtle issue with the dipole–dipole approximation is that it wrongly predicts symmetric excited-state couplings ($J_{D,xy} = J_{D,yx}$) between the same molecules from different unit cells, whose transition densities should couple in a nonsymmetric way ($J_{C,xy} \neq J_{C,yx}$).] Thus, the point-dipole approximation for computing excitonic couplings may not be reliable for modeling absorption spectra in these thin films, especially when employing 2D and 3D models.

6 Discussion & outlook

In this work, we implemented a tight-binding Frenkel exciton Hamiltonian with on-site energies and exciton coupling parameters obtained from TD-DFT calculations to model the low-temperature exciton absorption spectra of organic molecular thin films of H_2OBPc molecules. Our model allows us to systematically investigate the effect of different dimensionalities and exciton coupling at varied cutoff distances, thus providing a robust benchmark in the computational study of organic thin films.

A key advancement of our work lies in adapting and extending the theoretical formalism beyond the commonly explored 1D models,[29,65] which typically include one or two electronic states per molecule,[37] to handle 2D and 3D representations of the thin films. For our system, H_2OBPc crystalline thin films with a triclinic unit cell,[39] the molecules are found to form distorted hexagonal layers. Molecular thin films in two dimensions, most notably pentacene,[66,67] have been extensively characterized for their charge-transport properties, whereas theoretical treatments of the charge and exciton properties and their dynamics in phthalocyanine, remain scarce. As such, our framework opens new avenues for probing exciton dynamics and charge conduction in layered organic materials.

While 1D nearest neighbor models of H_2OBPc feature sharp absorption peaks, the extension to 2D/3D models and an incorporation of exciton couplings beyond the nearest neighbors lead to a broadening of the predicted spectra (especially when PBE0 functional is used to acquire Frenkel Hamiltonian elements) and a substantially larger splitting between the two main absorption peaks with the PBE0/3NN-26 Å model, which is in better agreement with experimental data. Our findings thus show the importance of adopting the proper dimensionality and including longer-range exciton coupling in modeling the spectral features of molecular aggregates. We also found that the point-dipole approximation for evaluating couplings between monomeric excitons generally exaggerates their

interactions and leads to overestimated peak splitting with pure functionals (such as PBE), thus this approximation should be used with caution.

Going beyond the Coulomb coupling, our direct coupling calculations[53] also produced Dexter exchange integrals between the transition density matrices, which were found for dimers A, B and C to be at least 100 times smaller than Coulomb coupling. So the Dexter contributions to the exciton absorption spectra are expected to be not substantial. As for charge transfer excitations, these excitations can occur between any pairs of molecules in a molecular crystal. Within the ALMO-TDA model,[68–70] we found that these charge transfer excitations have nearly zero oscillator strength even for A-, B- and C-dimers due to non-overlapping electron and hole densities on the two monomers. Furthermore, TD-DFT calculations on these dimers show that the charge transfer excitations do not mix with the local excitations considered so far in our work within the Frenkel–Davydov exciton model. Therefore, these excitations do not contribute to the exciton absorption spectra, either.

So far, our investigations have focused on the low-temperature regime. Work is underway to extend the theoretical models developed here to finite-temperature regimes. This will enable treatment exciton–phonon couplings, including effects of both local/static (Holstein)[30,71] and non-local/dynamic (Peierls) disorders[30,32,72] on the coherent exciton transport. This development is expected to provide critical insights into the energy-transfer mechanisms that control exciton transport in this class of organic materials.[17,30,73–78] For instance, while the simulated adsorption spectra do not change substantially upon the adding of more layers to the 3D model (see Fig. S14(j)–(l)), the exciton transport properties could be much more sensitive.

The H_2OBPc crystal is treated in this work using 1D, 2D, and 3D cluster models, where the on-site energies and exciton couplings are computed from TDDFT calculations on isolated molecules and direct coupling calculations on molecular dimers, respectively. Work is underway to use high-level wave-function methods, such as complete active state self-consistent field (CASSCF) theory[79] and complete active space second-order perturbation theory (CASPT2),[80,81] to check the accuracy of these on-site energies, transition densities, as well as Coulomb couplings.[82] We also note that the absorption spectra and other properties of molecular crystals have also been modeled with electrostatic embedding under the periodic boundary condition (PBC).[83] A future systematic comparison of the cluster and PBC approaches would be desirable.

Author contributions

SS, LB, MF, YS: conceptualization; SS, ZP, CL: software; SS, ZP, CL, CRW, YM: data curation and analysis; SS, CL, ST, LB, MF, YS: original draft preparation; all: manuscript editing; YS, PH, YZ, ST, MF: funding acquisition, resources, supervision.

7030 | Phys. Chem. Chem. Phys., 2026, 28, 7021–7034

This journal is © the Owner Societies 2026

Conflicts of interest

The authors declare that they have no conflicts of interest.

Data availability

Acknowledgements

Notes and references

1 J. H. Burroughes, D. D. C. Bradley, A. R. Brown, R. N. Marks, K. Mackay, R. H. Friend, P. L. Burns and A. B. Holmes, Light-emitting diodes based on conjugated polymers, *Nature*, 1990, **347**, 539–541.

2 M. A. Baldo, D. F. O'Brien, Y. You, A. Shoustikov, S. Sibley, M. E. Thompson and S. R. Forrest, Highly efficient phosphorescent emission from organic electroluminescent devices, *Nature*, 1998, **395**, 151–154.

3 S. R. Forrest, Ultrathin Organic Films Grown by Organic Molecular Beam Deposition and Related Techniques, *Chem. Rev.*, 1997, **97**, 1793–1896.

4 R. H. Friend, R. W. Gymer, A. B. Holmes, J. H. Burroughes, R. N. Marks, C. Taliani, D. D. C. Bradley, D. A. dos Santos, J.-L. Brédas, M. Lögdlund and W. R. Salaneck, Electroluminescence in conjugated polymers, *Nature*, 1999, **397**, 121–128.

5 M. C. J. M. Vissenberg and M. Matters, Theory of the field-effect mobility in amorphous organic transistors, *Phys. Rev. B:Condens. Matter Mater. Phys.*, 1998, **57**, 12964–12967.

6 H. Koezuka, A. Tsumura and T. Ando, Field-effect transistor with polythiophene thin film, *Synth. Met.*, 1987, **18**, 699–704.

7 B. S. Ong, Y. Wu, P. Liu and S. Gardner, High-Performance Semiconducting Polythiophenes for Organic Thin-Film Transistors, *J. Am. Chem. Soc.*, 2004, **126**, 3378–3379.

8 R. P. Xu, Y. Q. Li and J. X. Tang, Recent advances in flexible organic light-emitting diodes, *J. Mater. Chem. C*, 2016, **4**, 9116–9142.

9 L. Dou, Y. Liu, Z. Hong, G. Li and Y. Yang, Low-Bandgap Near-IR Conjugated Polymers/Molecules for Organic Electronics, *Chem. Rev.*, 2015, **115**, 12633–12665.

10 C. D. Sheraw, T. N. Jackson, D. L. Eaton and J. E. Anthony, Functionalized pentacene active layer organic thin-film transistors, *Adv. Mater.*, 2003, **15**, 2009–2011.

11 K. Kim, K. Nam, X. Li, D. Y. Lee and S. H. Kim, Programmed Design of Highly Crystalline Organic Semiconductor Patterns with Uniaxial Alignment via Blade Coating for High-Performance Organic Field-Effect Transistors, *ACS Appl. Mater. Interfaces*, 2019, **11**, 42403–42411.

12 Y. Xiao, W. Deng, J. Hong, X. Ren, X. Zhang, J. Shi, F. Sheng, X. Zhang and J. Jie, Water-Surface-Mediated Precise Patterning of Organic Single-Crystalline Films via Double-Blade Coating for High-Performance Organic Transistors, *Adv. Funct. Mater.*, 2023, **33**, 2213788.

13 H. Matsui, Y. Takeda and S. Tokito, Flexible and printed organic transistors: From materials to integrated circuits, *Org. Electron.*, 2019, **75**, 105432.

14 A. Khasbaatar, Z. Xu, J. H. Lee, G. Campillo-Alvarado, C. Hwang, B. N. Onusaitis and Y. Diao, From Solution to Thin Film: Molecular Assembly of π-Conjugated Systems and Impact on (Opto)electronic Properties, *Chem. Rev.*, 2023, **123**, 8395–8487.

15 G. Horowitz, Organic thin film transistors: From theory to real devices, *J. Mater. Res.*, 2004, **19**, 1946–1962.

16 V. Coropceanu, J. Cornil, D. A. da Silva Filho, Y. Olivier, R. Silbey and J. L. Brédas, Charge Transport in Organic Semiconductors, *Chem. Rev.*, 2007, **107**, 926–952.

17 J. L. Brédas, D. Beljonne, V. Coropceanu and J. Cornil, Charge-Transfer and Energy-Transfer Processes in π-Conjugated Oligomers and Polymers: A Molecular Picture, *Chem. Rev.*, 2004, **104**, 4971–5004.

This journal is © the Owner Societies 2026

Phys. Chem. Chem. Phys., 2026, **28**, 7021–7034 | **7031**

18 J. Zaumseil and H. Sirringhaus, Electron and Ambipolar Transport in Organic Field-Effect Transistors, *Chem. Rev.*, 2007, **107**, 1296–1323.

19 O. Ostroverkhova, Organic Optoelectronic Materials: Mechanisms and Applications, *Chem. Rev.*, 2016, **116**, 13279–13412.

20 M. Schwoerer and H. C. Wolf, *Organic Molecular Solids*, Wiley-VCH, Weinheim, 2008.

21 X. Xu, Z. Lou, S. Cheng, P. C. Y. Chow, N. Koch and H. M. Cheng, Understanding and Engineering the Interfacial Interaction in Organic/Inorganic van der Waals Heterostructures for (Opto)electronics, *Chem*, 2021, **7**, 2989–3026.

22 N. Rawat, Z. Pan, L. W. Manning, C. J. Lamarche, I. Cour, R. L. Headrick, R. Waterman, A. R. Woll and M. I. Furis, Macroscopic Molecular Ordering and Exciton Delocalization in Crystalline Phthalocyanine Thin Films, *J. Phys. Chem. Lett.*, 2015, **6**, 1834–1840.

23 S. C. J. Meskers, The Exciton Model for Molecular Materials: Past, Present and Future?, *ChemPhysChem*, 2023, **24**, e202300666.

24 H. Najafov, B. Lee, Q. Zhou, L. C. Feldman and V. Podzorov, Observation of long-range exciton diffusion in highly ordered organic semiconductors, *Nat. Mater.*, 2010, **9**, 938–943.

25 L. W. Manning, N. Rawat, C. Lamarche, R. Waterman, R. L. Headrick and M. Furis, Exciton Delocalization in H2OBPc1−xMOBPcx (M = Co, Cu, Ni, Mn) Crystalline Thin-Film Organic Alloys, *J. Phys. Chem. C*, 2016, **120**, 11966–11976.

26 L. Liang, K. Czar and M. I. Furis, Strain-Enhanced Formation of Delocalized Exciton States in Phthalocyanine Crystalline Thin Films, *J. Phys. Chem. C*, 2022, **126**, 8889–8896.

27 L. Liang, K. Burrill and M. I. Furis, Transition Dipole Moments of One-Dimensional Excitons in Soluble Phthalocyanine Thin Films, *J. Phys. Chem. C*, 2021, **125**, 27966–27974.

28 A. S. Davydov, *Theory of Molecular Excitons*, Springer, New York, 1971.

29 R. P. Fornari, J. Aragó and A. Troisi, Exciton Dynamics in Phthalocyanine Molecular Crystals, *J. Phys. Chem. C*, 2016, **120**, 7987–7996.

30 A. J. Sneyd, T. Fukui, D. Paleček, S. Prodhan, I. Wagner, Y. Zhang, J. Sung, S. M. Collins, T. J. A. Slater, Z. Andaji-Garmaroudi, L. R. MacFarlane, J. D. Garcia-Hernandez, L. Wang, G. R. Whittell, J. M. Hodgkiss, K. Chen, D. Beljonne, I. Manners, R. H. Friend and A. Rao, Efficient energy transport in an organic semiconductor mediated by transient exciton delocalization, *Sci. Adv.*, 2021, **7**, eabh4232.

31 S. Prodhan, S. Giannini, L. Wang and D. Beljonne, Long-Range Interactions Boost Singlet Exciton Diffusion in Nanofibers of π-Extended Polymer Chains, *J. Phys. Chem. Lett.*, 2021, **12**, 8188–8193.

32 S. Giannini, W. T. Peng, L. Cupellini, D. Padula, A. Carof and J. Blumberger, Exciton transport in molecular organic semiconductors boosted by transient quantum delocalization, *Nat. Commun.*, 2022, **13**, 2755.

33 F. C. Spano, The Spectral Signatures of Frenkel Polarons in H- and J-Aggregates, *Acc. Chem. Res.*, 2010, **43**, 429–439.

34 F. C. Spano, S. C. J. Meskers, E. Hennebicq and D. Beljonne, Probing Excitation Delocalization in Supramolecular Chiral Stacks by Means of Circularly Polarized Light: Experiment and Modeling, *J. Am. Chem. Soc.*, 2007, **129**, 7044–7054.

35 M. Kasha, Energy Transfer Mechanisms and the Molecular Exciton Model for Molecular Aggregates, *Radiat. Res.*, 1963, **20**, 55–70.

36 F. C. Spano and H. Yamagata, Vibronic Coupling in J-Aggregates and Beyond: A Direct Means of Determining the Exciton Coherence Length from the Photoluminescence Spectrum, *J. Phys. Chem. B*, 2011, **115**, 5133–5143.

37 N. J. Hestand and F. C. Spano, Expanded Theory of H- and J-Molecular Aggregates: The Effects of Vibronic Coupling and Intermolecular Charge Transfer, *Chem. Rev.*, 2018, **118**, 7069–7163.

38 F. C. Spano, J. Clark, C. Silva and R. H. Friend, Determining exciton coherence from the photoluminescence spectral line shape in poly(3-hexylthiophene) thin films, *J. Chem. Phys.*, 2009, **130**, 074904.

39 Y. Gao, Y. Chen, R. Li, Y. Bian, X. Li and J. Jiang, Nonperipherally Octa(butyloxy)-Substituted Phthalocyanine Derivatives with Good Crystallinity: Effects of Metal–Ligand Coordination on the Molecular Structure, Internal Structure, and Dimensions of Self-Assembled Nanostructures, *Chem. – Eur. J.*, 2009, **15**, 13241–13252.

40 M. E. Casida, *Recent Advances in Density Functional Methods Part I.*, World Scientific, 1995, p. 155.

41 M. E. Casida and M. Huix-Rotllant, Progress in Time-Dependent Density-Functional Theory, *Annu. Rev. Phys. Chem.*, 2012, **63**, 287–323.

42 S. Hirata and M. Head-Gordon, Time-Dependent Density Functional Theory for Radicals, *Chem. Phys. Lett.*, 1999, **302**, 375–382.

43 E. Epifanovsky, A. T. B. Gilbert, X. Feng, J. Lee, Y. Mao, N. Mardirossian, P. Pokhilko, A. F. White, M. P. Coons, A. L. Dempwolff, Z. Gan, D. Hait, P. R. Horn, L. D. Jacobson, I. Kaliman, J. Kussmann, A. W. Lange, K. U. Lao, D. S. Levine, J. Liu, S. C. McKenzie, A. F. Morrison, K. D. Nanda, F. Plasser, D. R. Rehn, M. L. Vidal, Z.-Q. You, Y. Zhu, B. Alam, B. J. Albrecht, A. Aldossary, E. Alguire, J. H. Andersen, V. Athavale, D. Barton, K. Begam, A. Behn, N. Bellonzi, Y. A. Bernard, E. J. Berquist, H. G. A. Burton, A. Carreras, K. Carter-Fenk, R. Chakraborty, A. D. Chien, K. D. Closser, V. Cofer-Shabica, S. Dasgupta, M. de Wergifosse, J. Deng, M. Diedenhofen, H. Do, S. Ehlert, P.-T. Fang, S. Fatehi, Q. Feng, T. Friedhoff, J. Gayvert, Q. Ge, G. Gidofalvi, M. Goldey, J. Gomes, C. E. González-Espinoza, S. Gulania, A. O. Gunina, M. W. D. Hanson-Heine, P. H. P. Harbach, A. Hauser, M. F. Herbst, M. Hernández Vera, M. Hodecker, Z. C. Holden, S. Houck, X. Huang, K. Hui, B. C. Huynh, M. Ivanov, Á. Jász, H. Ji, H. Jiang, B. Kaduk, S. Köhler,

7032 | *Phys. Chem. Chem. Phys.*, 2026, **28**, 7021–7034

This journal is © the Owner Societies 2026

K. Khistyaev, J. Kim, G. Kis, P. Klunzinger, Z. Koczor-Benda, J. H. Koh, D. Kosenkov, L. Koulias, T. Kowalczyk, C. M. Krauter, K. Kue, A. Kunitsa, T. Kus, I. Ladjánszki, A. Landau, K. V. Lawler, D. Lefrancois, S. Lehtola, R. R. Li, Y.-P. Li, J. Liang, M. Liebenthal, H.-H. Lin, Y.-S. Lin, F. Liu, K.-Y. Liu, M. Loipersberger, A. Luenser, A. Manjanath, P. Manohar, E. Mansoor, S. F. Manzer, S.-P. Mao, A. V. Marenich, T. Markovich, S. Mason, S. A. Maurer, P. F. McLaughlin, M. F. S. J. Menger, J.-M. Mewes, S. A. Mewes, P. Morgante, J. W. Mullinax, K. J. Oosterbaan, G. Paran, A. C. Paul, S. K. Paul, F. Pavošević, Z. Pei, S. Prager, E. I. Proynov, Á. Rák, E. Ramos-Cordoba, B. Rana, A. E. Rask, A. Rettig, R. M. Richard, F. Rob, E. Rossomme, T. Scheele, M. Scheurer, M. Schneider, N. Sergueev, S. M. Sharada, W. Skomorowski, D. W. Small, C. J. Stein, Y.-C. Su, E. J. Sundstrom, Z. Tao, J. Thirman, G. J. Tornai, T. Tsuchimochi, N. M. Tubman, S. P. Veccham, O. Vydrov, J. Wenzel, J. Witte, A. Yamada, K. Yao, S. Yeganeh, S. R. Yost, A. Zech, I. Y. Zhang, X. Zhang, Y. Zhang, D. Zuev, A. Aspuru-Guzik, A. T. Bell, N. A. Besley, K. B. Bravaya, B. R. Brooks, D. Casanova, J.-D. Chai, S. Coriani, C. J. Cramer, G. Cserey, A. E. DePrince, R. A. DiStasio, A. Dreuw, B. D. Dunietz, T. R. Furlani, W. A. Goddard, S. Hammes-Schiffer, T. Head-Gordon, W. J. Hehre, C.-P. Hsu, T.-C. Jagau, Y. Jung, A. Klamt, J. Kong, D. S. Lambrecht, W. Liang, N. J. Mayhall, C. W. McCurdy, J. B. Neaton, C. Ochsenfeld, J. A. Parkhill, R. Peverati, V. A. Rassolov, Y. Shao, L. V. Slipchenko, T. Stauch, R. P. Steele, J. E. Subotnik, A. J. W. Thom, A. Tkatchenko, D. G. Truhlar, T. Van Voorhis, T. A. Wesolowski, K. B. Whaley, H. L. Woodcock, P. M. Zimmerman, S. Faraji, P. M. W. Gill, M. Head-Gordon, J. M. Herbert and A. I. Krylov, Software for the frontiers of quantum chemistry: An overview of developments in the Q-Chem 5 package, *J. Chem. Phys.*, 2021, **155**, 084801.

44 J. P. Perdew, K. Burke and M. Ernzerhof, Generalized Gradient Approximation Made Simple, *Phys. Rev. Lett.*, 1996, **77**, 3865–3868.

45 C. Adamo and V. Barone, Toward reliable density functional methods without adjustable parameters: The PBE0 model, *J. Chem. Phys.*, 1999, **110**, 6158–6170.

46 C. Adamo, G. E. Scuseria and V. Barone, Accurate excitation energies from time-dependent density functional theory: Assessing the PBE0 model, *J. Chem. Phys.*, 1999, **111**, 2889–2899.

47 O. A. Vydrov, J. Heyd, A. V. Krukau and G. E. Scuseria, Importance of short-range versus long-range Hartree-Fock exchange for the performance of hybrid density functionals, *J. Chem. Phys.*, 2006, **125**, 074106.

48 J. D. Chai and M. Head-Gordon, Long-range corrected hybrid density functionals with damped atom–atom dispersion corrections, *Phys. Chem. Chem. Phys.*, 2008, **10**, 6615–6620.

49 R. Ditchfield, W. J. Hehre and J. A. Pople, Self-Consistent Molecular-Orbital Methods. IX. An Extended Gaussian-Type

Basis for Molecular-Orbital Studies of Organic Molecules, *J. Chem. Phys.*, 1971, **54**, 724–728.

50 W. J. Hehre, R. Ditchfield and J. A. Pople, Self—Consistent Molecular Orbital Methods. XII. Further Extensions of Gaussian-Type Basis Sets for Use in Molecular Orbital Studies of Organic Molecules, *J. Chem. Phys.*, 1972, **56**, 2257–2261.

51 P. C. Hariharan and J. A. Pople, The influence of polarization functions on molecular orbital hydrogenation energies, *Theor. Chim. Acta*, 1973, **28**, 213–222.

52 F. Plasser, A. I. Krylov and A. Dreuw, libwfa: Wavefunction analysis tools for excited and open-shell electronic states, *Wiley Interdiscip. Rev.:Comput. Mol. Sci.*, 2022, **12**, e1595.

53 C. P. Hsu, The Electronic Couplings in Electron Transfer and Excitation Energy Transfer, *Acc. Chem. Res.*, 2009, **42**, 509–518.

54 B. P. Krueger, G. D. Scholes and G. R. Fleming, Calculation of Couplings and Energy-Transfer Pathways between the Pigments of LH2 by the ab Initio Transition Density Cube Method, *J. Phys. Chem. B*, 1998, **102**, 5378–5386.

55 M. E. Madjet, A. Abdurahman and T. Renger, Intermolecular Coulomb Couplings from Ab Initio Electrostatic Potentials: Application to Optical Transitions of Strongly Coupled Pigments in Photosynthetic Antennae and Reaction Centers, *J. Phys. Chem. B*, 2006, **110**, 17268–17281.

56 K. A. Kistler, F. C. Spano and S. Matsika, A Benchmark of Excitonic Couplings Derived from Atomic Transition Charges, *J. Phys. Chem. B*, 2013, **117**, 2032–2044.

57 R. L. Headrick, S. Wo, F. Sansoz and J. E. Anthony, Anisotropic mobility in large grain size solution processed organic semiconductor thin films, *Appl. Phys. Lett.*, 2008, **92**, 063302.

58 S. Wo, R. L. Headrick and J. E. Anthony, Fabrication and characterization of controllable grain boundary arrays in solution-processed small molecule organic semiconductor films, *J. Appl. Phys.*, 2012, **111**, 073716.

59 Y. Li, J. Wan, D. M. Smilgies, N. Bouffard, R. Sun and R. L. Headrick, Nucleation and strain-stabilization during organic semiconductor thin film deposition, *Sci. Rep.*, 2016, **6**, 32620.

60 Z. Lu, C. Wang, W. Deng, M. T. Achille, J. Jie and X. Zhang, Meniscus-guided coating of organic crystalline thin films for high-performance organic field-effect transistors, *J. Mater. Chem. C*, 2020, **8**, 9133–9146.

61 M. Gouterman, Spectra of porphyrins, *J. Mol. Spectrosc.*, 1961, **6**, 138–163.

62 C. C. Wamser and A. Ghosh, The Hyperporphyrin Concept: A Contemporary Perspective, *JACS Au*, 2022, **2**, 1543–1560.

63 Y. Shao, Y. Mei, D. Sundholm and V. R. I. Kaila, Benchmarking the Performance of Time-Dependent Density Functional Theory Methods on Biochromophores, *J. Chem. Theory Comput.*, 2020, **16**, 587–600.

64 M. Caricato, G. W. Trucks, M. J. Frisch and K. B. Wiberg, Oscillator Strength: How Does TDDFT Compare to EOM-CCSD?, *J. Chem. Theory Comput.*, 2011, **7**, 456–466.

This journal is © the Owner Societies 2026

Phys. Chem. Chem. Phys., 2026, **28**, 7021–7034 | 7033

65 A. Troisi and G. Orlandi, Charge-Transport Regime of Crystalline Organic Semiconductors: Diffusion Limited by Thermal Off-Diagonal Electronic Disorder, *Phys. Rev. Lett.*, 2006, **96**, 086601.

66 S. Wang, Z. Wei, Y. Yang, X. Zhao, Q. Tang, Y. Tong and Y. Liu, Low surface energy interface-derived low-temperature recrystallization behavior of organic thin films for boosting carrier mobility, *J. Mater. Chem. C*, 2019, **7**, 13778–13785.

67 T. Salzillo, A. Brillante and A. Girlando, Terahertz Raman scattering as a probe for electron–phonon coupling, disorder and correlation length in molecular materials, *J. Mater. Chem. C*, 2021, **9**, 10677–10688.

68 Q. Ge, Y. Mao and M. Head-Gordon, Energy decomposition analysis for exciplexes using absolutely localized molecular orbitals, *J. Chem. Phys.*, 2018, **148**, 064105.

69 Q. Ge and M. Head-Gordon, Energy Decomposition Analysis for Excimers Using Absolutely Localized Molecular Orbitals within Time-Dependent Density Functional Theory and Configuration Interaction with Single Excitations, *J. Chem. Theory Comput.*, 2018, **14**, 5156–5168.

70 X. Ji, Z. Pei, K. N. Huynh, J. Yang, X. Pan, B. Wang, Y. Mao and Y. Shao, On the entanglement of chromophore and solvent orbitals, *J. Chem. Phys.*, 2025, **162**, 064107.

71 T. Holstein, Studies of polaron motion: Part I. The molecular-crystal model, *Ann. Phys.*, 1959, **8**, 325–342.

72 J. H. Fetherolf, D. Golež and T. C. Berkelbach, A Unification of the Holstein Polaron and Dynamic Disorder Pictures of Charge Transport in Organic Crystals, *Phys. Rev. X*, 2020, **10**, 021062.

73 T. Förster, 10th Spiers Memorial Lecture. Transfer mechanisms of electronic excitation, *Discuss. Faraday Soc.*, 1959, **27**, 7–17.

74 S. M. Menke and R. J. Holmes, Exciton diffusion in organic photovoltaic cells, *Energy Environ. Sci.*, 2014, **7**, 499–512.

75 S. Bai, P. Zhang and D. N. Beratan, Predicting Dexter Energy Transfer Interactions from Molecular Orbital Overlaps, *J. Phys. Chem. C*, 2020, **124**, 18956–18960.

76 O. P. Dimitriev, Dynamics of Excitons in Conjugated Molecules and Organic Semiconductor Systems, *Chem. Rev.*, 2022, **122**, 8487–8593.

77 S. Cao, A. Rosławska, B. Doppagne, M. Romeo, M. Féron, F. Chérioux, H. Bulou, F. Scheurer and G. Schull, Energy funnelling within multichromophore architectures monitored with subnanometre resolution, *Nat. Chem.*, 2021, **13**, 766–770.

78 D. L. Andrews, C. Curutchet and G. D. Scholes, Resonance energy transfer: Beyond the limits, *Laser Photonics Rev.*, 2011, **5**, 114–123.

79 P. A. Malmqvist and B. O. Roos, The CASSCF state interaction method, *Chem. Phys. Lett.*, 1989, **155**, 189–194.

80 J. Finley, P. A. Malmqvist, B. O. Roos and L. Serrano-Andrés, The multi-state CASPT2 method, *Chem. Phys. Lett.*, 1998, **288**, 299–306.

81 S. Battaglia and R. Lindh, On the role of symmetry in XDW-CASPT2, *J. Chem. Phys.*, 2021, **154**, 034102.

82 A. Kaiser, R. E. Daoud, F. Aquilante, O. Kühn, L. De Vico and S. I. Bokarev, A Multiconfigurational Wave Function Implementation of the Frenkel Exciton Model for Molecular Aggregates, *J. Chem. Theory Comput.*, 2023, **19**, 2918–2928.

83 M. Rivera, M. Dommett and R. Crespo-Otero, ONIOM(QM:QM) Electrostatic Embedding Schemes for Photochemistry in Molecular Crystals, *J. Chem. Theory Comput.*, 2019, **15**, 2504–2516.

7034 | *Phys. Chem. Chem. Phys.*, 2026, **28**, 7021–7034

This journal is © the Owner Societies 2026